Eur. Phys. J. Plus (2022) 137:1287
https://doi.org/10.1140/epjp/s13360-022-03411-1

THE EUROPEAN PHYSICAL JOURNAL PLUS

Regular Article

Study of fusion–fission dynamics in $^{12}C + ^{197}Au$ system

Pavneet Kaur, Moumita Maiti[a]

Department of Physics, Indian Institute of Technology Roorkee, Roorkee, Uttarakhand 247667, India

Received: 29 May 2022 / Accepted: 19 October 2022

Abstract A massive compound nucleus (CN) usually deexcites through light particle evaporation and fission. Scarcity available in the study of fusion–fission (FF) dynamics for the preactinide region nuclei pushed us to explore the reaction involving the fusion of ^{12}C with the ^{197}Au target at energies within 3.7–6.1 MeV/nucleon. After the bombardment, residues produced in each Au target were identified using the off-beam γ–ray spectroscopy method. Consequently, 10 evaporation residues (ERs) and 9 fission fragments within $85 \leq A \leq 167$ mass range, formed by complete fusion (CF)/incomplete fusion (ICF), have been confirmed through the activity measurements. PACE4 and EMPIRE3.2.2 reaction model codes were employed to analyze the measured cross sections of ERs, out of which PACE4 estimations were found to show relatively better agreement. The comparisons between measured and theoretical excitation functions ensured the absence of pre-compound processes within the studied energy range. At the same time, model-dependent calculations estimated 8.7% ICF strength at 72 MeV energy. Further, to get better insight into the dynamics, the mass distribution of fission fragments was examined. Broad and symmetric mass distribution observed through the Gaussian fitting gave evidence of the production of fission fragments through a compound nuclear mechanism. Also, the trend of mass variance with changing entrance channel parameters, precisely mass asymmetry, was examined. As a result, an almost linear increment of mass variance with an increasing value of mass asymmetry was spotted.

1 Introduction

Collision of two massive nuclei, a phenomenon termed as heavy-ion induced reaction, unlocks routes for multiple nuclear processes, which majorly involve complete-incomplete fusion evaporation [1–13], pre-equilibrium (PEQ) emissions [14–19], and fusion–fission. Earlier investigations have reported significant ICF contributions in the reactions involving ^{12}C projectile, even at energies within 4–8 MeV/nucleon [20–26]. ^{12}C, an α-clustered projectile with α separation energy of about 7.3 MeV, tends to split into ^{8}Be and α fragments. Fusion of either of these fragments with the target suppresses the CF contribution above the Coulomb barrier energies compared to the one-dimensional barrier penetration model or coupled-channels calculations. ICF study of more target-projectile combinations has been demanded in literature while interpreting the dependence of ICF fraction on various entrance-channel parameters, like projectile energy (E_{lab}), input angular momenta, mass asymmetry, Coulomb effect (Z_pZt), and Q_α values of projectiles [3, 25, 27–31]. Hence, experimental probing of this fact around the Coulomb barrier is still a matter of great interest.

The amalgamation of two heavy partners leads to such an enormous, excited, and/or rotating CN. Thus, the fission process starts competing strongly with the evaporation of particles during the de-excitation process. Fission fragment mass distribution (FFMD) is one of the fascinating post-fission observables for which extensive studies have been reported in the literature [15, 26, 32–38]. Dispersion parameters extracted from FFMD add knowledge about the spread of the mass distribution with changing E* [39–41]. Mass variance behavior with varying mass asymmetry has also been studied for different target-projectile combinations [33–36]. It is evident from the literature that the study of FF dynamics for the preactinide region, particularly for extremely neutron deficient ($1.15 \leq N/Z \leq 1.55$) nuclei, is minimal. Hence, we have made an effort to add some valuable information on the reaction mechanisms involved in the fusion of ^{12}C with ^{197}Au, which produces equilibrated CN ^{209}At with $N/Z = 1.46$.

It is important to note that several studies on the $^{12}C+ ^{197}Au$ system have been reported by different groups. Gordon *et al*. [42] studied the angular distribution for $^{12}C+ ^{197}Au$ system and extracted the fission cross sections by making some assumptions. Thomas et al. [43] and Bimbot et al. [44] reported cross section measurements for At, and Bi and Tl isotopes, respectively, through α activity detection, whereas Stickler and Hofstetter [45], and Baba et *al*. [46] reported *xn* channel excitation functions by measuring γ-ray activity. Further, in ref. [47], measurements of ref. [45] were compared with the statistical model calculations, which utilized the level density given by Weisskopf and Ewing [48]. Disagreement between the measured and theoretically estimated cross sections'

[a] e-mail: moumita.maiti@ph.iitr.ac.in (corresponding author)

Published online: 29 November 2022

magnitude was seen for each residue. Also, many of the isotopes' decay schemes were not firmly established at that time. Parker et al. [49] calculated differential recoil range distributions and cross sections at 120 MeV.

Vergani et al. [50] in 1993 reported the presence of PEQ above 80 MeV, but no satisfactory agreement between theory and the measurements was observed below this energy. This discrepancy was due to the assumptions made in the model calculations. The limitations of the theoretical model used in this study made it doubtful to come to any definite conclusions. Hence, it is crucial to compare the data with a reliable theoretical model to mark the presence or absence of PEQ below 80 MeV. Moreover, cross section measurements were done using half-life, characteristic γ energy, and abundance information from ref. [51], published in the year 1983. However, new updates for all the above quantities significantly affect the calculations. Hence, studying this system again is extremely important to explore the reaction mechanisms occurring below 80 MeV. It is crucial to note that we have incorporated popular theoretical model codes to estimate and compare the excitation functions for all the possible reaction channels. The principal motivation behind the present study is to comprehensively understand the different reaction processes contributing to the fusion of clustered structure projectile with the heavy-mass target within the chosen energy range.

The experimental details and theoretical calculations are presented in sects. 2 and 3, respectively. Section 4 represents the results of the present study and sect. 5 discusses the conclusions of the report.

2 Experimental details

^{12}C-ion beam having energy within 44–73 MeV in the laboratory frame of reference was utilized from the 14UD BARC-TIFR Pelletron Accelerator facility, Mumbai, India. The experiment was performed by using self-supporting natural Gold ^{197}(Au) targets prepared by the rolling method with a thickness of 3.5 mg/cm^2. Three stacks, each containing two sets of Au–Al foils, were irradiated by ^{12}C-ion beam. Behind each Gold foil, a backing of Aluminum foil (catcher) having a thickness within 1.5–1.8 mg/cm^2 was placed for energy degradation and catching the ERs in the forward beam direction. This arrangement of target and catcher is popularly known as the stacked-foil technique. SRIM (Stopping and Range of Ions in Matter) code [52] estimated energy degradation in each foil. The calculated energies at the center of each Au target came out to be 72 $\pm$ 1.6, 65.6 $\pm$ 1.7, 58.8 $\pm$ 1.8, 51.4 $\pm$ 1.9, and 44.2 $\pm$ 2.0 MeV. A constant beam current of ~ 10.5 pnA was maintained throughout the experiment, and the average beam flux was ~ 6.8 $\times$ 10^{10} particles/sec during the experiment.

Off-line γ-spectroscopy method [53, 54] was adopted in which a large volume high purity germanium detector was coupled with a PC-based multi-channel analyzer and GENIE-2K software to assay each target–catcher (Au–Al) set after the end of the bombardment (EOB). The detector with an energy resolution of 2.0 keV at 1332 keV γ-ray of ^{60}Co was precalibrated by using the standard sources, ^{152}Eu (13.517 y), ^{137}Cs (30.08 y), and ^{60}Co (5.27 y) of known activity. Each residue was identified based on its characteristic γ-rays and decay profiles. The spectroscopic data [55] of the identified ERs and fission fragments are represented in Table 1 and Table 2, respectively.

The cross section calculations have been done using the relation mentioned in ref. [26]. Several factors responsible for the uncertainty in the cross section measurement and energy have been taken into account during the calculations. These factors include uncertainty in the efficiency calibration of the detector ($\leq$ 2%), measurement of target thickness (2%), and beam flux (6–7%). Moreover, statistical error in the background-subtracted peak area count and error in estimating beam energy due to energy degradation while passing through successive target-catcher foils were also considered to estimate the total uncertainty associated with the cross section measurements. However, energy straggling was assumed to be less.

3 Theoretical calculations

Theoretical model codes PACE4 [57] and EMPIRE3.2.2 [58] have been used within 56–90 MeV incident energy range to estimate the cross sections of residues produced in ^{12}C+ ^{197}Au reaction. The core goal of comparing theoretical estimations with experimental data is to understand the reaction mechanism. Below is a brief description of the used statistical codes and their input parameter information.

PACE4 works in the framework of LISE++ and traces the decay of an excited CN using the Monte Carlo Method. It is based on the Hauser-Feshbach (HF) formalism for compound nuclear evaporation and considers the energy conservation and angular momentum at each stage of the particle evaporation. For light particle emissions (like n, p, and α), transmission coefficients were determined from optical model calculations where default optical model parameters were taken from ref. [59]. Bass model [60] was used to calculate compound nuclear fusion cross sections and initial spin distributions. Considering fission as a decay mode, PACE4 used a modified rotating liquid drop fission barrier given by A.J. Sierk [61] to estimate it. The level density parameter is defined as α A/K, where A is the mass number of CN, and K is the free parameter whose value may be varied. In the present study, we have used K= 9 and 10. The ratio,α_f /α_n, where α_f and α_n are the level density parameters for fission and neutron emissions, is taken as unity. PACE4 does not account for direct (DIR) processes and PEQ emissions, and only total production cross section information can be estimated for each residue.

Table 1 Spectroscopic data [55] of the radionuclides formed through CF/ICF processes in $^{12}C+ ^{197}Au$ system

Nuclides	J^{π}	Decay mode (%)	Half-life	Eγ(keV)	Iγ(%) [Uncertainty]
^{206}At	5^{+}	$\epsilon^{a} + \beta^{+}$ (99.10)	30.6 min	395.54	48.0 [3]
		α (0.90)		477.1	86 [4]
				700.66	97.6 [-]
$^{205}At^{b}$	$9/2^{-}$	$\epsilon + \beta^{+}$ (90.00)	26.2 min	520.44	4.41 [18]
		α (10.00)		669.41	8.6 [4]
				719.3	31.0 [-]
$^{204}At^{b}$	7^{+}	$\epsilon + \beta^{+}$ (96.2)	9.2 min	516.318	90.0 [3]
		α (3.8)		684.341	95.0 [3]
^{205}Po	$5/2^{-}$	$\epsilon + \beta^{+}$ (99.96)	1.74 h	836.8	19.1 [12]
		α (0.04)		849.8	25.4 [12]
				872.4	36.8 [-]
				1001.2	28.7 [12]
				1239.1	4.6 [3]
^{204}Po	0^{+}	$\epsilon + \beta^{+}$ (99.33)	3.519 h	137.023	11.1 [3]
		α (0.67)		270.068	31.9 [11]
				1016.29	27.6 [7]
^{204}Bi	6^{+}	$\epsilon + \beta^{+}$ (100)	11.22 h	374.76	82.0 [8]
				899.15	99.0 [12]
				983.98	59.0 [6]
^{202}Bi	5^{+}	$\epsilon + \beta^{+}$ (100)	1.71 h	422.13	83.7 [25]
				657.49	60.6 [18]
				960.67	99.283 [-]
^{201}Bi	$9/2^{-}$	$\epsilon + \beta^{+}$ (100)	103 min	629.1	26.0 [17]
				786.4	10.3 [7]
				818.9	8.0 [5]
				936.2	12.2 [8]
				1325.2	6.6 [4]
^{201}Pb	$5/2^{-}$	$\epsilon + \beta^{+}$ (100)	9.33 h	331.15	77.0 [6]
^{198}Tl	7^{+}	$\epsilon + \beta^{+}$ (55.9)	1.87 h	411.8	59.0 [6]
		IT^{c} (44.1)			

[a]Electron capture
[b]γ-ray information has been taken from ref. [56]
[c]Isomeric transition

Table 2 Spectroscopic data [55] of the fission fragments formed in $^{12}C+ ^{197}Au$ system

Nuclides	J^{π}	Decay mode (%)	Half-life	Eγ(keV)	Iγ(%) [Uncertainty]
^{85}Kr	$1/2^{-}$	β^{-} (78.8)	4.48 h	151.195	75.2 [5]
		IT (21.2)			
^{95}Ru	$5/2^{+}$	$\epsilon + \beta^{+}$ (100)	1.643 h	806.28	4.04 [17]
^{109}In	$9/2^{+}$	$\epsilon + \beta^{+}$ (100)	4.159 h	948.9	1.45 [5]
^{117}Sb	$5/2^{+}$	$\epsilon + \beta^{+}$ (100)	2.8 h	158.562	85.9 [-]
^{120}Xe	0^{+}	$\epsilon + \beta^{+}$ (100)	40 min	555.6	1.45 [22]
$^{129}Ba^{a}$	$7/2^{+}$	$\epsilon + \beta^{+}$ (< 100)	2.16 h	1078.0	1.4^{b} [11]
$^{156}Ho^{a}$	4^{-}	$\epsilon + \beta^{+}$ (100)	56 min	366.25	10.73 [10]
^{163}Tm	$1/2^{+}$	$\epsilon + \beta^{+}$ (100)	1.81 h	471.33	4.05 [14]
^{167}Ho	$7/2^{-}$	β^{-} (100)	3.1 h	346.5	57.0 [-]

[a]γ-ray information has been taken from ref. [56]
[b]Relative intensity

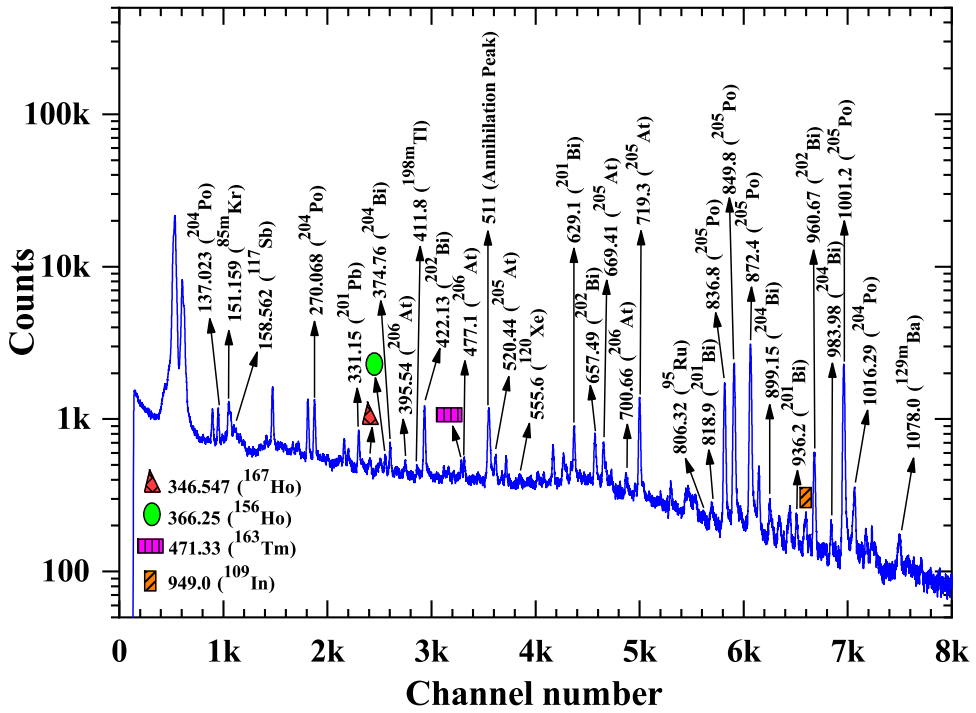

Fig. 1 A typical γ-ray spectrum of ^{197}Au irradiated by $E_{lab} = 72$ MeV ^{12}C beam, collected after 1.3 h of EOB. The energy of γ-ray peaks is in keV

EMPIRE3.2.2 accounts for all three major nuclear reaction formalisms, namely, DIR, PEQ, and EQ. It uses either the coupled-channels approach or distorted wave Born approximation (DWBA) to calculate DIR processes. HF model is used for the compound reaction process. Since the exciton model is popular for PEQ emission calculations, we have used it with a mean free path parameter value of 1.5. The optical model is used for fission calculations and coupled-channels calculation (CCFUS) [62] is used for heavy-ion fusion cross section. Nuclear masses, optical model parameters, ground-state deformations, discrete levels and decay schemes, level densities, fission barriers, and γ-ray strength functions are internally provided by input library RIPL- 3 [63]. In the present study, the experimental data are compared with EMPIRE3.2.2 estimations obtained by incorporating Gilbert-Cameron (GC) [64] level density model. It considers nuclei's collective (rotational/vibrational) effect on nuclear level density.

4 Results and discussion

Residual radionuclides produced in the ^{12}C+ ^{197}Au reaction at different incident energies have been identified by analyzing the γ–ray spectra collected from each Au-Al set after the EOB. This process ensured the production of ^{206}At, ^{205}At, ^{204}At, ^{205}Po, ^{204}Po, ^{204}Bi, ^{202}Bi, ^{201}Bi, ^{201}Pb, and ^{198m}Tl in the target matrix. Moreover, de-excitation of massive CN also led to the production of ^{85m}Kr,^{95}Ru, ^{109}In, ^{117}Sb, ^{120}Xe, ^{129}Ba, ^{156}Ho, ^{163}Tm, and ^{167}Ho residues through fission. A γ–ray spectrum of 72 MeV ^{12}C irradiated ^{197}Au, collected after 1.3 h of the EOB, is shown in Fig. 1, and the characteristic γ-peaks corresponding to each residue have been marked. The marking of extra peaks belonging to pre-marked residues has been avoided to maintain the clarity of the spectrum. The half-life estimation method has been adopted to get confirmation of residues. The background-subtracted and dead-time corrected peak area of each residue's characteristic γ–rays have been analyzed to measure the activity and hence the residual cross section (σ) using the activation formula, detail of which is available in ref. [26]. Table 3 represents the calculated cross sections for the residues populated through CF and ICF at various energies. It is crucial to note that our measurement did not see any ER or fission product for the below barrier incident energies, 51.4 and 44.2 MeV.

4.1 Residual cross section

4.1.1 xn channel

Production of three radionuclides $^{206, 205, 204}$, At, through the evaporation of neutrons from CN, has been confirmed in the observed γ–ray spectra. Figure 2a shows the excitation function of ^{206}At, produced through ^{197}Au(^{12}C, 3n) reaction. The trend of excitation functions for refs. [46, 50] and the present study resembles. However, the magnitude of cross sections reported by ref. [50] is higher than our measurements. It is also observed that, for the lowest energy point, at 58.8 MeV, our cross section data are satisfactorily

Table 3 Cross section (mb) of evaporation residues and fission fragments at various incident energies

	Cross section (mb)		
Residues(↓)			
E_{lab}(MeV)(→)	72 ± 1.6	65.6 ± 1.7	58.8 ± 1.8
E *c.m* (MeV)(→)	67.9 ± 1.5	61.8 ± 1.6	55.4 ± 1.7
^{85m}Kr	4.4 ±0.6	2.4 ± 0.4	–
^{95}Ru	34.0 ±11.3	24.9 ±6.8	–
^{109}In	386.1 ±63.6	274.6 ± 47.2	–
^{177}Sb	0.95 ±0.2	0.8 ± 0.2	–
^{120}Xe	111.2 ±30.6	199.0 ± 43.2	–
$_{120m}$Ba	271.6 ±45.1	112.0 ± 25.0	–
^{156}Ho	22.6 ±4.3	20.5 ± 3.6	–
^{165}Tm	48.8 ±9.2	19.5 ± 4.9	–
^{167}Ho	3.8 ±0.8	–	–
^{206}At	10.1 ±2.3	36.9 ± 4.9	6.7 ± 0.9
^{205}At	362.1±46.2	184.4 ± 25.0	2.7 ± 0.5
^{204}At	13.2 ±1.8	–	–
^{205}Po$_{cum}$	385.1 ±41.2	184.3 ± 20.2	3.3 ± 0.6
^{204}Po$_{cum}$	39.3 ±5.4	–	–
^{204}Bi$_{cum}$	15.8±2.3	–	–
^{202}Bi	24.8 ±3.4	6.7 ± 0.9	–
^{204}Bi	38.0 ±6.0	19.1 ± 3.4	0.7 ± 0.2
202Pb$_{cum}$	16.1 ±2.5	9.2 ± 1.4	–
^{198}Tl	2.2±0.5	0.9± 0.3	–

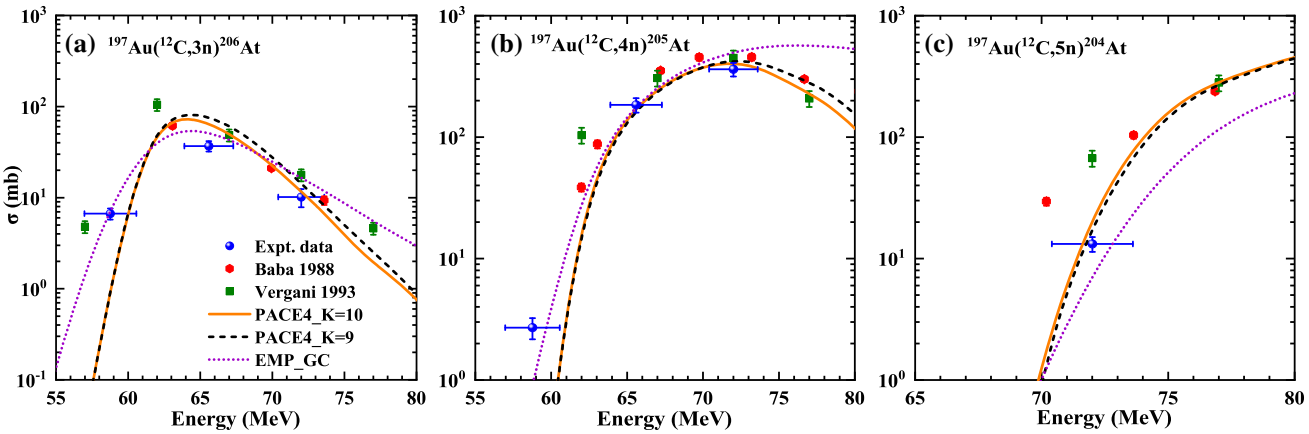

Fig. 2 Comparison of measured excitation function of (**a**)^{206}At, (**b**) ^{205}At, and (**c**) ^{204}At with theoretical predictions from PACE4 and EMPIRE3.2.2 (denoted by EMP), and the data reported by 'Baba 1988' [46] and 'Vergani 1993' [50]

reproduced by EMPIRE3.2.2 with level density GC, whereas, for higher energy points, it is overpredicting the data. On the other hand, PACE4 with K=9 and 10 efficiently explains our measurements rather than EMPIRE3.2.2 at the higher energy region. It ensures the absence of PEQ emissions in this channel as PACE4 computation is based only on the HF formalism, which purely accounts for the equilibrium mechanism.

The excitation function of ^{205}At produced through ^{197}Au(^{12}C, 4n) reaction is shown in Fig. 2b. The cross sections reported in refs. [46] and [50] are larger than our measurements. EMPIRE3.2.2 satisfies our measurements below 70 MeV, within the uncertainty limit. Contrary to this, except for the lowest energy point, PACE4 predictions are in good agreement with our experimental data. It claims the occurrence of only compound nuclear process in this case. Figure 2c represents the comparison of measured cross sections and theoretical excitation functions for ^{204}At. It is evident from Fig. 2(c) that our data are close to the theoretical estimations of PACE4. However, the data reported in ref. [46, 50] are higher than our measurements and theoretical results, below 75 MeV incident energy.

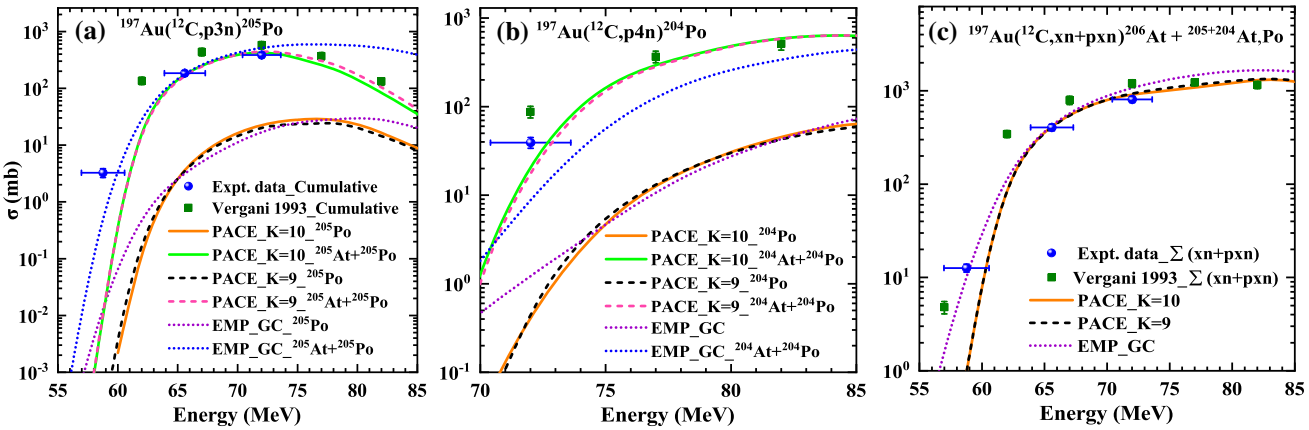

Fig. 3 Comparison of measured excitation function of (**a**) ^{205}Po, (**b**) ^{204}Po, and (**c**) $^{206+205+204}$ At + $^{205+204}$Po with theoretical predictions and the data reported by 'Vergani 1993' [50]

Collectively viewing the *xn*-channel observations, we can state that our measurements are more likely explainable by the theoretical predictions. It is essential to notice that the lowest energy point, i.e., 58.8 MeV, lies below the Coulomb barrier. Hence, EMPIRE, which incorporates the coupled-channels calculation, can estimate cross sections adequately in the lower energy region rather than PACE4, which utilizes the one-dimensional barrier penetration model. Moreover, the absence of PEQ can be noted in the present work within the energy range studied.

4.1.2 pxn channel

Excitation functions of ^{205}Po and ^{204}Po can be seen in Fig. 3(a) and 3(b), respectively. Large disagreement between our measurements and the predictions from PACE4 and EMPIRE indicates the possibility of the feeding of these residues through their short-lived precursors ^{205}At (26.2 min) and ^{205}At (9.2 min), respectively. Hence, production of ^{205}Po and ^{204}Po can take place directly through *p3n* and *p4n* channels, respectively, as well as indirectly through the decay of their precursors. Therefore, the experimentally measured cross sections of ^{205}Po and ^{204}Po are cumulative. Acknowledging this fact, we have compared the measured ^{205}Po cross sections with the sum of ^{205}At and ^{205}Po cross sections obtained from PACE4 and EMPIRE. Figure 3(a) reveals that above the Coulomb barrier, PACE4 is more efficiently explaining the measurements instead of EMPIRE. Cross sections reported by ref. [50] are significantly larger than our measurements and PACE4 with K=10. Similar observations have been made in the case of ^{204}Po below 75 MeV, as shown in Fig. 3(b). The observed enhancement in Vergani *et al*. [50] data for similar energy can be explained based on the different intensity information used while calculating cross sections. Here also, the sum of ^{204}At and ^{204}Po cross sections obtained from PACE4 is satisfying the cumulative cross section of ^{204}Po.

The sum of experimentally measured excitation functions of all the *xn* and *pxn* reaction channel residues is compared with the sum of theoretical excitation functions, as shown in Fig. 3(c). PACE4 is satisfactorily reproducing our measurements, while EMPIRE is unable to reproduce the data apart from the lowest incident energy. Also, the sum of *xn* and *pxn* reaction channel cross sections deduced from ref. [50] can be observed to have higher cross sections than our measurements and theoretical predictions within the overlapping energy range. It has been observed throughout the comparison of ref. [50] data with theoretical estimations that at the high energy region, above 75 MeV, the cross sections become consistent with PACE4. However, it is higher in magnitude than the predictions below this energy range, where our measurements are seen to be successfully explainable by PACE4 with $K = 10$. Therefore, the measured excitation functions of the remaining residues have been compared with it.

4.1.3 α-emitting channels

Figure 4(a) represents the comparison of our measured cross section with Bimbot et al. [44] and theoretical estimations of PACE4 for ^{204}Bi, produced through ^{197}Au(^{12}C, α) reaction. The cross section value reported by ref. [44] shows a considerable enhancement than our measurement at 72 MeV, and PACE4 underpredicts the measurements. The reason behind such observation might be the provision of getting only independent cross section information through PACE4. It is important to note that ^{204}Bi can also be produced indirectly through the decay of ^{204}Po $\rightarrow$ ^{204}Bi; also, ^{204} Po can be produced indirectly through the decay of ^{204}At $\rightarrow$ ^{204}Po. Thus, we have compared our measured cumulative cross section with the sum of ^{204}At, ^{204}Po, and ^{204}Bi cross sections obtained from PACE4. Consequently, a good agreement between them has been observed, as shown in Fig. 4(a). Cumulative cross sections reported by ref. [44] are also satisfying the predictions made by PACE4, except for energies below 75 MeV. Also, only the maximum limit of cross section has been reported by ref. [44], marked in Fig. 4(a) for 68.8 MeV energy. Generally, enhancement in the cross sections

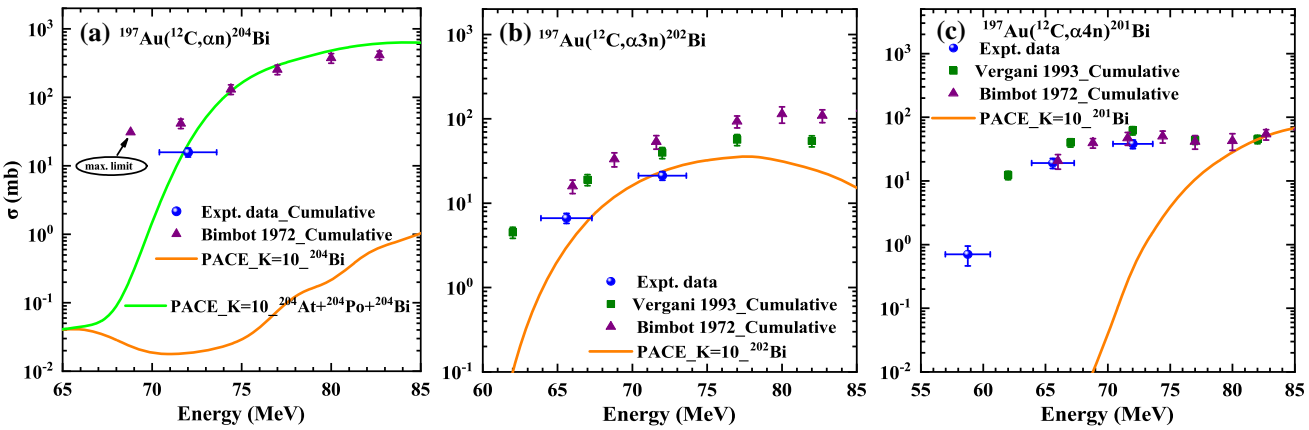

Fig. 4 Comparison of measured excitation function of (**a**)^{204}Bi, (**b**) ^{202}Bi, and (**c**) ^{201}Bi with theoretical estimations of PACE4 and the data reported by 'Bimbot 1972' [44] and 'Vergani 1993' [50]

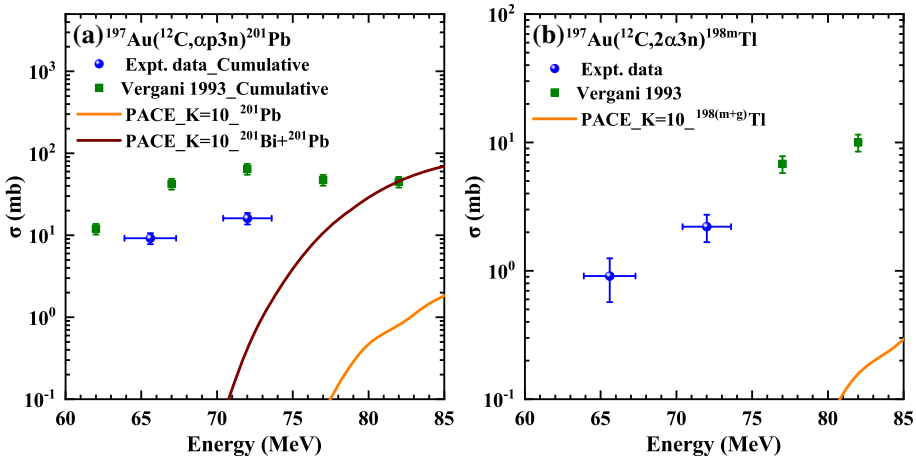

Fig. 5 Comparison of measured excitation function of (**a**) ^{201}Pb and (**b**) ^{198m}Tl with theoretical estimations of PACE4 and the data reported by 'Vergani 1993' [50]

in the α-emitting channels is regarded as the contribution from ICF along with the CF process. However, after including feeding of ^{204}Bi through its precursors, no further enhancement has been observed; it indicates the absence of ICF in this channel.

The excitation function of ^{202}Bi is represented in Fig. 4(b). PACE4 is reproducing our data well, within the uncertainty limit. However, large cross sections have been reported by refs. [44] and [50]. We have reported independent cross sections, as ^{202}At and ^{202}Po precursors have not been identified in this study. Contrary to this, refs. [44] and [50] both have reported cumulative cross sections for ^{202}Bi. It is worth noticing that the indistinguishability of our measurements with theoretical predictions from PACE4 has marked the absence of ICF in ^{202}Bi residue and provided the information that it is producing independently during the fusion of ^{12}C with ^{197}Au. One might also remember that variations in cross section sometimes arrive due to different intensity values. In the present case, for 422 keV characteristic γ energy, ref. [44] used a much lower intensity, 66%, than the presently used value 83.7%. Comparing independent cross sections rather than cumulative and incorporating the latest intensity information in the calculations might lead to the agreement between the earlier reported data and the theoretical estimations, indicating the absence of ICF.

Measured cross sections for ^{201}Bi can be observed in Fig. 4(c). Our measurements are consistent with the previously reported data [44], whereas cross sections of ref. [50] are larger than ours. After comparing it with PACE4, significant enhancement of experimental data has been observed. The Isomeric Transition of ^{201m}Bi to ^{201}Bi with branching ratio $\leq$ 8.6% might be responsible for the large cross section values. However, the characteristic γ energy for ^{201m}Bi (846.4 keV) has not been identified in the present system. Hence, we cannot consider it a reason responsible for the enhancement in the cross section. The decay of ^{201}At into ^{201}Po and then its decay into ^{201}Bi might also be the reason for drastic increment in the cross sections. However, since none of the precursors has been identified in the present study, ICF of ^{12}C into ^{197}Au might be considered a major reason behind the observed enhancement. Thus, the production of ^{201}Bi may be attributed to CF and ICF channels. Substantially low cross section estimations by PACE4 imply the production of the residue dominantly through the ICF process.

In the case of Pb, a comparison of experimental data with ref. [50] and PACE4 calculations can be observed in Fig. 5(a). Since the half-life of ^{201}Bi (103 min) is relatively less than ^{201}Pb (9.33 h), its production through the decay of ^{201}Bi $\rightarrow$ ^{201}Pb could be expected. Therefore, we have compared our cumulative cross section data with the sum of ^{201}Bi and ^{201}Pb cross sections obtained from PACE4. Regardless of this, at 65.6 MeV, PACE4 alone is not even showing any possibility for the production of ^{201}Pb. Moreover,

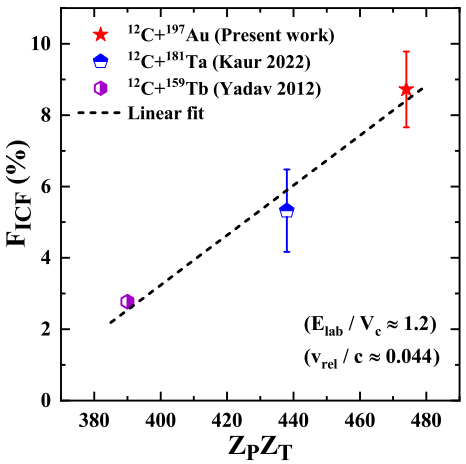

Fig. 6 Comparison of the ICF fraction of the present system with 'Kaur 2022' [26] and 'Yadav 2012' [22] at normalized energy with $v_{rel}/c \sim 0.044$

significant enhancement can still be remarked, indicating the extra cross section contribution through the ICF process. Similar observations have been accounted for ref. [50] data.

In order to confirm the non-existence of ICF in the case of ^{204}Bi and ^{202}Bi residues, PACE4 calculations have been performed for ^{8}Be+ ^{197}Au reaction. Consequently, the possibility of the formation of these residues was found to be negligible. It might be the reason for marking no trace of ICF for both residues in the present study. Contrary to this, PACE4 estimated significant cross sections for ^{201}Bi (4n channel) and ^{201}Pb (p3n channel) during the fusion of ^{8}Be with ^{197}Au target. This observation hinted at ICF expectations in the present study for ^{201}Bi and ^{201}Pb residues, as noticeable in Figs. 4(c) and 5(a).

In the case of ^{198m}Tl, Vergani *et al*. [50] reported cross section data above 75 MeV, at a higher energy range compared to the present data, represented in Fig. 5(b). However, we have compared the measured ^{198m}Tl cross sections with PACE4, which only estimates total cross section information. Hence, it is clear that the theoretical predictions made by PACE4 are the upper limit of cross sections obtained for^{198}(g+m) Tl residue. Despite this, the estimations are underpredicting the reported data in ref. [50], and it does not even show the production of ^{198}(g+m) Tl residue within our experimental energy range. It indicates that ^{198}(g+m) Tl residue's production comes through the ICF process. In summary, ^{201}Bi, ^{201}Pb, and ^{198m}Tl might have been produced through the following possible reaction channels:

(i) Complete fusion channel: The CF of ^{12}C with ^{197}Au results in the formation of ^{209}At* CN, which leads to the production of ^{201}Bi, ^{201}Pb, and ^{198m}Tl through α 4n, α p3n, and 2α 3n channel, respectively.

$$^{12}\mathrm{C} + {}^{197}\mathrm{Au} \rightarrow {}^{209}\mathrm{At}^{*} \rightarrow {}^{201}\mathrm{Bi} + \alpha 4n,\ \mathrm{E_{th}} = 47.1\ \mathrm{MeV} \tag{1}$$

$$^{12}\mathrm{C} + {}^{197}\mathrm{Au} \rightarrow {}^{209}\mathrm{At}^{*} \rightarrow {}^{201}\mathrm{Pb} + \alpha p3n,\ \mathrm{E_{th}} = 42.2\ \mathrm{MeV} \tag{2}$$

$$^{12}\mathrm{C} + {}^{197}\mathrm{Au} \rightarrow {}^{209}\mathrm{At}^{*} \rightarrow {}^{198m}\mathrm{Tl} + 2\alpha 3n,\ \mathrm{E_{th}} = 34.7\ \mathrm{MeV} \tag{3}$$

(ii) Incomplete fusion channel: ^{12}C being cluster structured is prone to its break up into fragments in the presence of sufficient projectile energy and with the influence of nuclear force field, as shown below:

$$^{12}\mathrm{C} \rightarrow {}^{8}\mathrm{Be} + \alpha,\ Q_{\mathrm{value}} = -7.4\ \mathrm{MeV} \tag{4}$$

$$^{12}\mathrm{C} \rightarrow {}^{8}\mathrm{Be} + \alpha,\ Q_{\mathrm{value}} = -7.4\ \mathrm{MeV} \tag{5}$$

The possible breakups of the projectile mentioned above would lead to the formation of ^{201}Bi, ^{201}Pb, and ^{198m}Tl when one of the fragments fuses with the target and the other fragment moves in the forward direction as a spectator. Specifically, fusion of ^{8}Be fragment with ^{197}Au target might lead to the formation of ^{201}Bi, ^{201}Pb, and ^{198m}Tl through 4n, $p3n$, and α3n channel, respectively. Similarly, fusion of αfragment with ^{197}Au target might produce ^{198m}Tl through 3n channel.

$$^{8}\mathrm{Be} + {}^{197}\mathrm{Au} \rightarrow {}^{205}\mathrm{Bi}^{*} \rightarrow {}^{201}\mathrm{Bi} + 4n, \mathrm{E_{th}} = 38.6\ \mathrm{MeV} \tag{6}$$

$$^{8}\mathrm{Be} + {}^{197}\mathrm{Au} \rightarrow {}^{205}\mathrm{Bi}^{*} \rightarrow {}^{201}\mathrm{Pb} + p3n, \mathrm{E_{th}} = 33.7\ \mathrm{MeV} \tag{7}$$

$$^{8}\mathrm{Be} + {}^{197}\mathrm{Au} \rightarrow {}^{205}\mathrm{Bi}^{*} \rightarrow {}^{198m}\mathrm{Tl} + \alpha 3n, E_{\mathrm{th}} = 26.3\ \mathrm{MeV} \tag{8}$$

$$\alpha + {}^{197}\mathrm{Au} \rightarrow {}^{201}\mathrm{Tl}^{*} \rightarrow {}^{198m}\mathrm{Tl} + 3n, E_{\mathrm{th}} = 25.9\ \mathrm{MeV} \tag{9}$$

(iii) β^+ emission and/or ε decay of precursor: Along with CF and ICF processes, the decay of precursor (^{201}Bi) through β emission and/or ε might also contribute to the production of ^{201}Pb residue.

$$^{201}\mathrm{Bi}^{*} \rightarrow {}^{201}\mathrm{Pb} + \beta^{+}/\epsilon, \tag{10}$$

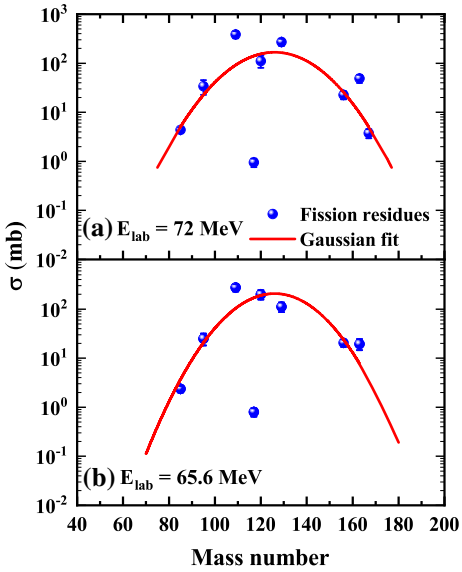

Fig. 7 FFMD at different incident energies. A solid line represents the Gaussian fit

Theoretical models do not consider ICF in the calculations, which might be why the observed underprediction of cross sections in the α-emitting channels. In contrast, these models with the same input parameters were observed to satisfy the *xn* channel measurements grossly. PACE4 is unable to predict the possibility of formation of the majority of the residues produced through α-emitting channels for which we have measured large cross sections. Hence, we only got the opportunity to calculate the ICF strength ($F_{\rm ICF}$) at the highest energy point, at 72 MeV. Since, from Fig. 2, it is evident that PACE4 with K=10 is more efficiently reproducing our measurements, we have taken it as a reference for the $F_{\rm ICF}$ calculations. It is defined as, $F_{\rm ICF}$ (%) = ($\sum \sigma_{\rm ICF}/\sigma_{\rm TF}^{\rm theor}$)× 100%, where $\sum \sigma_{\rm ICF} = \sum \sigma_{TF(\rm expt)}^{^{201}\rm Bi+^{201}Pb_{cum}} - \sum \sigma_{\rm CF(PACE4)}^{^{201}\rm Bi+^{201}Pb_{cum}}$ and σ_{TF}^{theor} is the total theoretical fusion cross section predicted by PACE4. Consequently, these purely model-dependent calculations resulted in 8.7 ± 1.1% of $_{\rm ICF}$ at 72 MeV. It is worth mentioning that the cross sections of stable residues and radionuclides having weak γ-rays and very short half-lives are not measured due to the limitations of the adopted technique. Hence, the $_{\rm ICF}$ reported for the present data can be considered as its lowest limit.

Further, in order to see the dependence of $E_{\rm ICF}$ on target mass, we have compared the$E_{\ \rm ICF}$ for the present system with the $^{12+}$C^{181}Ta [26] and ^{12}C+^{159}Tb [22] system, shown in Fig. 6, at normalized energy value $E_{\rm Lab}/{\rm v_c}$ ~ 1.2 corresponding to $v_{\rm rel}/{\rm c}$ = 0.044 value [65], where v_c represents the Coulomb barrier in lab frame of reference. Linear increment in $E_{\rm ICF}$ with increasing $Z_{\rm p}$ $Z_{\rm T}$, a product of atomic numbers of the projectile and target nuclei, has been observed. It suggests that the increasing $Z_{\rm p}Z_{\rm T}$ value, which implies the rising strength of the Coulomb interaction, enhances the magnitude of projectiles' breakup probability which eventually raises the ICF strength. The three systems chosen for the comparison have a common projectile, i.e., ^{12}C, so the variation of ICF strength with changing mass asymmetry at normalized energy is also expected to show a similar trend as observed in Fig. 6.

4.2 Mass distribution of fission fragments

The study of fission fragment mass distribution provides information regarding FF dynamics. The distribution is expected to be single-peaked in Gaussian shape for compound nuclear fission. In the present work, a total of 9 fission radionuclides within the mass range 85 ≤A≤ 167 have been identified from γ-spectra recorded from each Au-Al set. It is crucial to mention that for ^{129}Ba, absolute intensity information is not available in the databases [55, 56]. Therefore, we have performed the cross section calculations for this particular residue using relative intensity. Moreover, for ^{163}Tm, the calculations have been done considering 471.33 keV γ peak with Iγ = 4.05%, but there are two neighboring peaks to this $E\gamma$, namely, 469.65 (Iγ = 0.4%) and 473.76 (Iγ = 0.2%) keV. Hence, there might be a possibility of their contribution to the cross section calculations; still, it would be minimal due to their much less intensity value compared to the chosen characteristic γ. The measured cross sections of the fission fragment at 72 MeV and 65.6 MeV are recorded in Table 3. By summing the individual cross sections of fission fragments, the total fission cross sections have been found as 883.4 ± 85.1 and 653.6 ± 69.3 mb at $E_{\rm lab}$ = 72 MeV and 65.6 MeV, respectively. These measurements are much higher than the fission cross section predictions made by PACE4 and EMPIRE. A similar observation regarding large deviations between theoretical estimations and experimentally measured fission cross sections has been found in the literature [15, 26].

Figure 7 represents the experimentally measured individual cross sections of the fission fragments populated in the ^{12}C+^{197}Au reaction as a function of mass number. A broad and symmetric mass distribution is acquired for both energies, which indicates the formation of fission fragments from the compound nuclear mechanism. Hence, the independent yield is represented as:

$$Y(A) = ae^{\frac{-(A-M_{mp})^2}{2\sigma_m^2}} \tag{11}$$

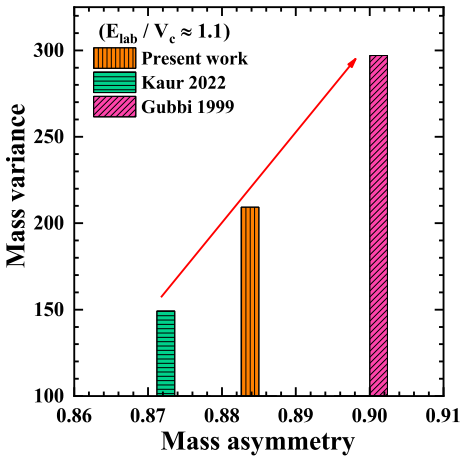

Fig. 8 Comparison of mass variance of present work with 'Kaur 2022' [26] and 'Gubbi 1999' [32] at normalized energy E_{lab} /V_c

where a, M_{mp}, and σ_m are the peak amplitude, most probable mass (centroid), and width parameter, respectively, obtained from the Gaussian distribution. Dispersion parameters (M_{mp},σ_m) have been extracted as (126, 15.5) at E_{lab} = 72 MeV and (126, 14.5) at E_{lab} = 65.6 MeV. The variance $\sigma^2{}_m$of the mass distribution has been found to be 241 u_2 at E_{lab} = 72 MeV (E^* = 49.6 MeV) and 209 u^2 at E_{lab} = 65.6 MeV (E^* = 43.6 MeV). It is evident that $\sigma^2{}_m$ is increasing with increasing E^*, hence, indicating the broadening of FFMD as we go to higher E^*. Similar behavior of raising variance with rising E^* is also reported in ref. [26, 33, 35, 36].

It is essential to mention that one data point belonging to ^{117}Sb, in Fig. 7, is far from the Gaussian fittings. Regardless of being confirmed through half-life measurement, which came out to be 2.7 h, close to its actual value, 2.8 h [55], significantly low cross sections have been obtained for it. As the cross section calculations have been carried out by adopting a similar procedure that has been followed for other fission fragment residues, no visible reason could be found for such low cross sections in the case of ^{117}Sb. However, this unexpected point hardly plays any role in extracting the dispersion parameter information as it has been ignored during the Gaussian fitting. So, the fission information is independent of this data point. Calculations of maximum input angular momentum (l_{max}) also have been done for both the E^* values and found to be 18$\hbar$ and 28$\hbar$ for E^* = 43.6 and 49.6 MeV, respectively. It has been observed that with increasing E^*, l^{max} is rising, which lowers the fission barrier (B_F) and eventually increases the fission cross section.

Moreover, in order to understand the role of entrance-channel mass asymmetry, $\alpha = (A^T\text{-}AP)/(A^T\text{+}AP)$, on the mass distribution of fission fragments, an attempt has been made. In this regard, the variance of FFMD reported in ref. [26] for ^{12}C+^{181}Ta system and ref. [32] for ^{11}B+^{232}Th system has been compared with the present system, ^{12}C+ ^{197}Au, as a function of α. Figure 8 represents the comparison for different target–projectile combinations mentioned above, at E_{Lab}/$V_c$value around 1.1. It provides clear observation regarding the linear increment in mass variance with increasing mass asymmetry. A similar trend has been reported in ref. [26, 33, 36] at fixed E_{Lab}/V_c value. A study of $\sigma^2 m$ over a wide range of α values would help in understanding its dependence on α.

5 Conclusion

In the present article, an effort has been made to comprehensively inspect the reaction processes occurring in the ^{12}C+ ^{197}Au system. For this, excitation functions for the identified ERs produced through CF and/or ICF processes have been compared with the theoretical model codes PACE4 and EMPIRE. The HF formalism-based PACE4 grossly agrees with the measured cross sections of *xn* channel residue, which implies the production of those radionuclides through the CF mechanism, hence, ensuring the absence of PEQ emissions. However, previous studies [49, 50] have reported the presence of PEQ emissions at relatively higher energies for the same system. While comparing our measurement with previously reported data, a similarity in the trend of the excitation functions has been noted along with variation in cross sections' magnitude. The primary reason behind this observation is the poor intensity information of most of the characteristic γ energies. In the α–emitting channels, relatively large cross sections compared to theory indicate the presence of the ICF process. At the highest measured energy point, 72 MeV, the F_{ICF} came out to be 8.7%. A rising trend of F_{ICF} with increasing coulomb effect also has been observed. Moreover, the possibility for the production of fission fragments has been reported with relatively higher fission cross sections than theory. Calculated L_{max} at 72 MeV and 65.6 MeV helped understand the increasing fission cross section with increasing excitation energy of the CN. The FFMD at different E^* is broad and symmetric, indicating that the CN's de-excitation follows the fission process. For the first time, FFMD and dispersion parameters, precisely the most probable mass and width parameters, have been reported for this system. The influence of entrance-channel parameters, namely mass asymmetry, on mass variance has been observed for E_{lab}/V_c ~ 1.1 value, and variance is found to be rising. Overall,

we must point out that, in the present study, we have successfully identified the expected processes, evaporation and fusion–fission, in a single experiment, which was not attempted yet.

Acknowledgements We sincerely thank the BARC-TIFR Pelletron team for their assistance during the experiment. We also appreciate our colleagues from TASISPEC Lab, IIT Roorkee, India, for their help and passionate teamwork. Student research fellowship from the University Grants Commission (UGC), Government of India, is gratefully acknowledged.

Availability of data and materials The cross section data are available and have already been reported explicitly in tables in the article.

Declarations

Conflict of interest There is no competing interest to the best of our knowledge.

References

1. J. Rangel, M.R. Cortes, J. Lubian, L.F. Canto, Phys. Lett. B **803**, 135337 (2020)
2. R. Prajapat, M. Maiti, Phys. Rev. C **101**, 024608 (2020)
3. A. Yadav, P.P. Singh, M. Shuaib, V.R. Sharma, I. Bala, D.P. Unnati, M.K. Singh, R. Sharma, S. Kumar, R.P. Murlithar, B.P. Singh, R. Prasad, Phys. Rev. C **96**, 044614 (2017)
4. P.P. Singh, A. Yadav, D.P. Singh, U. Gupta, M.K. Sharma, R. Kumar, D. Singh, R.P. Singh, S. Muralithar, M.A. Ansari, B.P. Singh, R. Prasad, R.K. Bhowmik, Phys. Rev. C **80**, 064603 (2009)
5. R. Prajapat, M. Maiti, Phys. Rev. C **103**, 034620 (2021)
6. I. Tserruya, V. Steiner, Z. Fraenkel, P. Jacobs, D.G. Kovar, W. Henning, M.F. Vineyard, B.G. Glagola, Phys. Rev. Lett. **60**, 14 (1988)
7. R. Prajapat, M. Maiti, Phys. Rev. C **101**, 064620 (2020)
8. D.P. Singh, P.P Unnati, A. Singh, M.K. Yadav, B.P Sharma, K.S. Singh, R. Golda, A.K. Kumar, R. Sinha, R. Prasad, Phys. Rev. C **81**, 054607 (2010)
9. U. Gupta, P.P. Singh, D.P. Singh, M.K. Sharma, A. Yadav, R. Kumar, B.P. Singh, R. Prasad, Nucl. Phys. A **811**, 77 (2008)
10. D. Kumar, M. Maiti, S. Lahiri, Phys. Rev. C **96**, 014617 (2017)
11. R. Kharab, R. Chahal, R. Kumar, Nucl. Phys. A **946**, 1 (2016)
12. D. Kumar, M. Maiti, Phys. Rev. C **96**, 044624 (2017)
13. M. Shuaib, V.R. Sharma, A. Yadav, M.K. Sharma, P.P. Singh, D.P. Singh, R. Kumar, R.P. Singh, S. Muralithar, B.P. Singh, R. Prasad, Phys. Rev. C **98**, 014605 (2018)
14. M. Blann, Nucl. Phys. A **235**, 211 (1974)
15. R. Prajapat, M. Maiti, D. Kumar, Phys. Rev. C **103**, 014608 (2021)
16. D. Kumar, M. Maiti, S. Lahiri. Phys. Rev. C **94**, 044603 (2016)
17. A. Chauhan, M. Maiti, S. Lahiri. Phys. Rev. C **99**, 064609 (2019)
18. M.K. Sharma, P.P. Singh, D.P. Singh, A. Yadav, V.R. Sharma, I. Bala, R. Kumar, Unnati, B.P. Singh, R. Prasad, Phys. Rev. C **91**, 014603 (2015)
19. R. Prajapat, M. Maiti, D. Kumar, A. Chauhan, Phys. Scr. **95**, 055306 (2020)
20. S. Mukherjee, A. Sharma, S. Sodaye, A. Goswami, B.S. Tomar, Int. J. Mod. Phys. E **15**, 237 (2006)
21. H. Kumar, S.A. Tali, M.A. Ansari, D. Singh, R. Ali, K. Kumar, N.P.M. Sathik, S. Parashari, A. Ali, R. Dubey*et al.*, Nucl. Phys. A **960**, 53 (2017)
22. A. Yadav, V.R. Sharma, P.P. Singh, D.P. Singh, M.K. Sharma, U. Gupta, R. Kumar, B.P. Singh, R. Prasad, R.K. Bhowmik, Phys. Rev. C **85**, 034614 (2012)
23. S. Chakrabarty, B.S. Tomar, A. Goswami, G.K. Gubbi, S.B. Manohar, A. Sharma, B. Bindukumar, S. Mukherjee, Nucl. Phys. A **678**, 355 (2000)
24. S. Gupta, B.P. Singh, M.M. Musthafa, H.D. Bhardwaj, R. Prasad, Phys. Rev. C **61**, 064613 (2000)
25. S.A. Tali, H. Kumar, M.A. Ansari, A. Ali, D. Singh, R. Ali, P.K. Giri, S.B. Linda, R. Kumar, S. Parashari, S. Muralithar, R.P. Singh, Phys. Rev. C **100**, 024622 (2019)
26. P. Kaur, M. Maiti, T.N. Nag, S. Sodaye, Phys. Rev. C **105**, 014629 (2022)
27. M. Shuaib, V.R. Sharma, A. Yadav, P.P. Singh, M.K. Sharma, D.P. Singh, R. Kumar, R.P. Singh, S. Muralithar, B.P. Singh, R. Prasad, Phys. Rev. C **94**, 014613 (2016)
28. H. Kumar, S.A. Tali, M.A. Ansari, D. Singh, R. Ali, A. Ali, S. Parashari, P.K. Giri, S.B. Linda, R. Kumar, R.P. Singh, S. Muralithar, Phys. Rev. C **99**, 034610 (2019)
29. D. Singh, P.K. Giri, A. Mahato, S.B. Linda, H. Kumar, M.A. Ansari, R. Ali, S.A. Tali, M.H. Rashid, R. Guin, S.K. Das, Nucl. Phys. A **981**, 75 (2019)
30. V.R. Sharma, A. Yadav, P.P. Singh, D.P. Singh, S. Gupta, M.K. Sharma, I. Bala, R. Kumar, S. Murlithar, B.P. Singh, R. Prasad, Phys. Rev. C **89**, 024608 (2014)
31. S.A. Tali, H. Kumar, M.A. Ansari, A. Ali, D. Singh, R. Ali, P.K. Giri, S.B. Linda, S. Parashari, R. Kumar, R.P. Singh, S. Muralithar, Nucl. Phys. A **970**, 208 (2018)
32. G.K. Gubbi, A. Goswami, B.S. Tomar, A. Ramaswami, A.V.R. Reddy, P.P. Burte, S.B. Manohar, B. John, Phys. Rev. C **59**, 3224 (1999)
33. M. Shuaib, V.R. Sharma, A. Yadav, S. Thakur, M.K. Sharma, I. Majeed, M. Kumar, P.P. Singh, D.P. Singh, R. Kumar, R.P. Singh, S. Muralithar, B.P. Singh, R. Prasad, Phys. Rev. C **99**, 024617 (2019)
34. V.R. Sharma, A. Yadav, P.P. Singh, M.K. Sharma, D.P. Singh, Unnati, R. Kumar, K.S. Golda, B.P. Singh, A.K. Sinha, R. Prasad, Phys. Rev. C **84**, 014612 (2011)
35. A. Sood, P.P. Singh, R.N. Sahoo, P. Kumar, A. Yadav, V.R. Sharma, M. Shuaib, M.K. Sharma, D.P. Singh, U. Gupta, R. Kumar, S. Aydin, B.P. Singh, H.J. Wollersheim, R. Prasad, Phys. Rev. C **96**, 014620 (2017)
36. V.R. Sharma, R. Kumar, S. Mukherjee, E.F. Aguilera, M. Shuaib, P.P. Singh, A. Yadav, R. Dubey, S. Appannababu, J.C. Morales-Rivera, S. Kumar, B.P. Singh, R. Prasad, Phys. Rev. C **99**, 034617 (2019)
37. G.S. Karapetyan, A. Deppman, V. Guimaraes, A. Balabekyan, N.A. Demekhina, Phys. Rev. C **94**, 024618 (2016)
38. S.S. Rattan, A. Ramaswami, S.B. Manohar, J. Radioanal. Nucl. Chem. **242**, 551 (1999)

39. R. Dubey, P. Sugathan, A. Jhingan, G. Kaur, I. Mukul, G. Mohanto, D. Siwal, N. Saneesh, T. Banerjee, M. Thakur, R. Mahajan, N. Kumar, M.B. Chatterjee, Phys. Lett. B **752**, 338 (2016)
40. T.K. Ghosh, S. Pal, K.S. Golda, P. Bhattacharya, Phys. Lett. B **627**, 26 (2005)
41. L.M. Pant, R.K. Choudhury, A. Saxena, D.C. Biswas, Eur. Phys. J. A **11**, 47 (2001)
42. G.E. Gordon, A.E. Larsh, T. Sikkeland, G.T. Seaborg, Phys. Rev. **120**, 1341 (1960)
43. T.D. Thomas, G.E. Gordon, R.M. Latimer, G.T. Seaborg, Phys. Rev. **126**, 1805 (1962)
44. R. Bimbot, D. Gardes, M.F. Rivet, Nucl. Phys. A **189**, 193 (1972)
45. J.D. Stickler, K.J. Hofstetter, Phys. Rev. C **9**, 1064 (1974)
46. S. Baba, K. Hata, S. Ichikawa, T. Sekine, Y. Nagame, A. Yokoyama et al., Z Phys. A **331**, 53 (1988)
47. K.J. Hofstetter, J.D. Stickler, Phys. Rev. C **9**, 1072 (1974)
48. V.F. Weisskopf, D.H. Ewing, Phys. Rev. **57**, 472 (1940)
49. D.J. Parker, P. Vergani, E. Gadioli, J.J. Hogan, F. Vettore, E. Gadioli-Erba, E. Fabrici, M. Galmarini, Phys. Rev. C **44**, 1528 (1991)
50. P. Vergani, E. Gadioli, E. Vaciago, E. Fabrici, E.G. Erba, M. Galmarini, G. Ciavola, C. Marchetta, Phys. Rev. C **48**, 1815 (1993)
51. U. Reus, W. Westmeier, At. Data Nucl. Data Tables **29**, 1 (1983)
52. J.F. Ziegler, M.D. Ziegler, J.P. Biersack, Nucl. Instrum. Methods Phys. Res. B **268**, 1818 (2010)
53. M. Sagwal, M. Maiti, T.N. Nag, S. Sodaye, Eur. Phys. J. Plus **136**, 1057 (2021)
54. R. Kumar, M. Maiti, T.N. Nag, S. Sodaye, Phys. Rev. C **104**, 064606 (2021)
55. http://www.nndc.bnl.gov/nudat2/ (National Nuclear Data Center, Brookhaven National Laboratory)
56. S. Y. F. Chu, L. P. Ekström, R. B. Firestone, The Lund/LBNL Nuclear Data Search: WWW Table of Radioactive Isotopes, http://nucleardata.nuclear.lu.se/toi/
57. A. Gavron, Phys. Rev. C **21**, 230 (1980)
58. M. Herman, R. Capote, B.V. Carlson, P. Oblozinsky, M. Sin, A. Trkov, H. Wienke, V. Zerkin, Nucl. Data Sheets **108**, 2655 (2007)
59. C.M. Perey, F.G. Perey, At. Data Nucl. Data Tables **17**, 1 (1976)
60. R. Bass, Phys. Rev. Lett. **39**, 265 (1977)
61. A.J. Sierk, Phys. Rev. C **33**, 2039 (1986)
62. C.H. Dasso, S. Landowne, Comput. Phys. Commun. **46**, 187 (1987)
63. R. Capote, M. Herman, P. Oblozinsky, P.G. Young, S. Goriely, T. Belgya, A.V. Ignatyuk, A.J. Koning, S. Hilaire, V. A. Plujko et al., Nucl. Data Sheets **110**, 3107 (2009)
64. A. Gilbert, A.G.W. Cameron, Can. J. Phys. **43**, 1446 (1965)
65. H. Morgenstern, W. Bohen, W. Galster, K. Grabisch, A. Kyanowski, Phys. Rev. Lett. **52**, 1104 (1984)